1   **Sub-3 Å resolution structure of apoferritin using a multi-purpose TEM with a side-entry**

2   **cryo-holder**

3

4   Yoko Kayama[$,1,2] Raymond N. Burton-Smith[$,1], Chihong Song[1], Naoya Terahara[3], Takayuki

5   Kato[4], Kazuyoshi Murata[1*]

6

7   [1]National Institute for Physiological Sciences, Okazaki, Aichi, 444-8585, Japan, [2]Terabase Inc.,

8   Okazaki, Aichi, 444-0864, Japan, [3]Faculty of Science and Engineering, Chuo University,

9   Bunkyoku, Tokyo, 112-8551, Japan, [4]Institute for Protein Research, Osaka University, Suita,

10   Osaka, 565-0871, Japan

11

12   [$]These authors contributed equally

13   [*]Correspondence: kazum@nips.ac.jp

14

15   **Summary**

16   The structural analysis of protein complexes by cryo-electron microscopy (cryo-EM) single

17   particle analysis (SPA) has had great impact as a biophysical method in recent years. Many results

18   of cryo-EM SPA are based on state-of-the-art cryo-electron microscopes customized for SPA.

19   These are currently only available in limited locations around the world, where securing machine

20   time is highly competitive. One potential solution for this time-competitive situation is to reuse

21   existing multi-purpose equipment. Here, we used a multi-purpose TEM with a side entry cryo-

22   holder at our facility to evaluate the potential of high-resolution SPA. We report a 3 Å resolution

23   map of apoferritin with local resolution extending to 2.6 Å. The map clearly showed two positions

24   of an aromatic side chain. We also verified the optimal imaging conditions depending on different

25   electron microscope and camera combinations. This study demonstrates the possibilities of more

26   widely available and established electron microscopes, and their applications for cryo-EM SPA.

27

28   **Keywords**

29   apoferritin; benchmarking; cryo-electron microscopy; multi-purpose TEM; single particle

30   analysis; side-entry cryo-holder

31

32 **Introduction**

33 Cryo-electron microscopy (cryo-EM) single particle analysis (SPA) is a technique for

34 reconstructing the three-dimensional structure of a biomacromolecule using projected images

35 acquired with an electron microscope (Bhella, 2019) and was the subject of the Nobel Prize for

36 Chemistry in 2017 (Cressey and Callaway, 2017). The technique has achieved tremendous

37 progress by integrating various technologies (Murata and Wolf, 2018).

38 Developments contributing to advances in SPA have been mainly improvements of electron

39 microscope performance (Knapek et al., 1982; Morishita et al., 2013), developments of electron

40 beam direct detectors (Bammes et al., 2012; McMullan et al., 2016), methods for three-

41 dimensional structure reconstructions (Grant et al., 2018; Kimanius et al., 2016; Punjani et al.,

42 2017; Zivanov et al., 2018), and automated acquisition via Leginon (Carragher et al., 2000),

43 SerialEM (Mastronarde, 2005) or manufacturer software. In recent years, close to atomic

44 resolution has been achieved (Bartesaghi et al., 2015; Danev et al., 2019; Kato et al., 2019) which

45 permits construction of atomic models without foreknowledge of the protein sequence.

46 All the above-mentioned techniques are indispensable for improving achieved resolution.

47 However, focusing on the performance of the electron microscope, including electron source, the

48 sample stage, and the detector is arguably the primary limiting factor. For example, autoloader

49 stages such as those used in Titan Krios (Thermo Fisher Scientific) and CRYOARM (JEOL)

50 microscopes demonstrate that multiple sample grids can be stored stably for a long period of time,

51 the sample grid can be automatically transported, and data can be automatically collected without

52 manual intervention. Such a sample stage is difficult to introduce later into a multi-purpose

53 electron microscope and is currently only available pre-installed. Such electron microscopes are

54 very expensive and are currently only available at limited locations. As a result, competition for

55 machine time is high. One solution is to reuse established equipment.

56 Optimisations of the microscope for SPA are often incompatible or non-ideal for other

57 techniques for which the microscope could be used, such as electron tomography (Baumeister,

58 2002), EDS (Allen et al., 2012), EELS (Egerton, 2009), STEM (Crewe et al., 1970) and microED

59 (Nannenga and Gonen, 2019). Nevertheless, the vast cost of maintaining multiple pieces of

60 optimised equipment precludes general availability. Therefore, it is desirable to be aware of how

61 realistic mid- to high-resolution SPA is on multi-purpose TEMs.

62   While datasets exceeding 1,000 micrographs are now regularly collected (Iudin et al., 2016),
63   this is unrealistic for manual data collection. Therefore, in this study, limited datasets (<200
64   micrograph movies each) were manually collected with a test specimen of apoferritin on two
65   microscope-and-detector combinations which serve as multi-purpose (S)TEMs, both using Gatan
66   626-type cryo-specimen holders. Apoferritin (Richter, 1959; Toussaint et al., 2007) is a relatively
67   recent addition to the "benchmark" samples for cryo-EM, since its compact size, spherical shape
68   and octahedral symmetry presented difficulties in reconstructing at lower resolutions (Russo and
69   Passmore, 2014). Using a beta release of RELION 3.1 and <300 micrograph movies, a 3 Å (global)
70   resolution map of apoferritin was achieved. We further examined optimized data collection
71   conditions for each general purpose cryo-EM setting, although as early datasets here had been
72   processed with RELION 3.0, we chose to continue processing these datasets with RELION 3.0,
73   rather than introduce a further variable. The limited number of acquired micrographs is intended
74   to offset the multiplicative effect of high symmetry on particle count and provide some indication
75   of utility on lower symmetry datasets.

76   While not all multi-purpose TEMs are equipped with automation software, the decrease in
77   workload for the microscope operator presented by automation, combined with the ability to
78   collect data more quickly makes software-controlled data acquisition highly desirable. To
79   demonstrate the utility of automation on data collection with a multi-purpose TEM which still
80   requires manual cryogen maintenance, we acquired a dataset of β-galactosidase using SerialEM,
81   post-installed automated software (Mastronarde, 2005) and processed independently. As a result,
82   3.6 Å resolution map was able to be acquired with one semi-automated session of data collection
83   that took six hours with two replenishments of liquid nitrogen.

84   In this work we provide a possibility to reuse existing equipment for high-resolution cryo-EM
85   and guidelines for the minimum setup for growth of the research field within general-access
86   facilities.

87

88   **Results**

89

90   **3 Å resolution map reconstruction using a multi-purpose TEM with a side-entry cryo-**

91   **holder**

92   With a limited dataset of 279 micrograph movies and using a beta version of RELION 3.1, we

93   achieved 3 Å (global) resolution of apoferritin (Fig. 1) when estimated at the gold-standard (GS)

94   (fully independent half-maps) FSC (0.143) (Fig. S1A) using a combination of JEM-2100F electron

95   microscope and K2 Summit direct electron detector (DED). Local resolution estimated by the

96   *blocres* module of Bsoft (Heymann, 2001; Heymann and Belnap, 2007) shows significant areas of

97   the map between 2.6-2.8 Å (Fig. 1A). All helices were clearly defined (Fig. 1A, B) with some

98   residues exhibiting two conformational states (Fig. 1B, marked with black arrows) although with

99   one conformation dominant as the second was lost at higher map σ (Fig. S1B). In higher resolution

100 regions side chains are clear (Fig. 1C) and densities could be assigned to metal atoms coordinated

101 by side chains (Fig. 1B, 1C, marked with red arrow). It may be possible to assign water to some

102 densities, but we erred on the side of caution with respect to interpreting potential water-related

103 density.

104

105 **Imaging comparison of two DEDs**

106 Photographs of one EM setup (Setting A; JEM-2100F, K2 Summit DED and Gatan 626 side entry

107 cryo-specimen holder) are shown in Fig. S2. The second (Setting B; JEM-2200FS, DE-20 DED

108 and Gatan 626 cryo-holder) has been shown previously (Murata and Wolf, 2018). Micrograph

109 movies independently collected from the two EM setups were corrected for image drift and

110 electron beam damage using the MotionCor2 algorithm (Zheng et al., 2017) as implemented in

111 RELION 3 (Zivanov et al., 2018). Table 1 details the essential information for each equipment

112 setting.

113   For comparison, representative cryo-EM images from each setup are shown in Fig. 2. In this

114 figure, images were captured at 50,000× magnification and displayed at the same particle scale. In

115 both cases, the projected image of apoferritin particles was easily recognized with similar contrast.

116 An area of the same absolute size as the image obtained with Setting A (K2 Summit detector)

117 acquisition is shown on the Setting B (DE-20 detector) micrograph by a white dashed box (Fig.

118 2B), highlighting the difference in field of view. The total number of apoferritin particles in the

119   example images were counted, totalling 383 in the Setting A image and 1,334 in the Setting B

120   image (Fig. 2).

121   We calculated the MTF and DQE curves (Fig. S3) in each case at 200kV using a beam stopper

122   and the FindDQE program (Ruskin et al., 2013), where the greatest difference between the curves

123   was shown in the low frequencies. The calculated DQE value at lower special frequencies was

124   >80% for the K2 Summit, but was reduced to ~35% when using the DE-20. At frequencies above

125   ¾ Nyquist, the two detectors have very similar response curves (Fig. S3). They show similar

126   characteristics to the same DEDs on different microscopes (Faruqi and McMullan, 2018; Kuijper

127   et al., 2015; Ruskin et al., 2013) as expected.

128   When comparing Setting A and Setting B using Pt-Ir film (Hamaguchi et al., 2019) (Fig. S4)

129   the clarity of Thon rings in Setting A is immediately apparent in the power spectrum (Fig. S4A)

130   and in the rotational average profile (Fig. S4B) to beyond the diffraction ring of 2.27 Å. Both

131   Settings were observed at 100,000× magnification, at which point Setting B is difficult to keep

132   stable. This is manifest in the weaker oscillations in the CTF and diffraction ring at ~2.3 Å (Fig.

133   S4C). Minor astigmatism of approximately 60 nm causes the blurring of the diffraction ring in

134   Setting B upon rotational averaging, which while visible in the power spectrum is not as clear in

135   the radial profile (Fig. S4D).

136

137   **Comparison of 3D reconstruction maps in different imaging conditions**

138   Eight cryo-EM maps of apoferritin with resolutions between 3.3 Å and 5.1 Å were obtained by

139   standard operation (Fig. 3) of RELION 3.0 using different data sets as detailed in Table 2. In all

140   final post-processing steps, a very soft mask (15 Å low-pass filter, 5 pixel expansion and 10 pixel

141   soft edge) was used, which slightly reduces the resolution estimated by "gold-standard" FSC (GS-

142   FSC) (Chen et al., 2013) than when a less soft mask was used. We would prefer to underestimate

143   the GS-FSC resolution than overestimate. Local resolution is unaffected by this softer mask.

144   Using limited datasets described in Table 2, the highest resolution map was obtained from a

145   data set acquired with Setting A at a magnification of 50,000×. The map coloured by local

146   resolution (Heymann, 2001; Heymann and Belnap, 2007) is shown in Fig. S5. The best local

147   resolution of ~2.8 Å was shown in the α-helices located inside the core. On the other hand, the

148   disordered N-terminal of each subunit showed the lowest resolution of ~3.6 Å.

149   A crystal structure model (PDBID: 2CIH) (Toussaint et al., 2007) was fitted to the map and a

150   single helix was extracted from each reconstruction to visualize map quality (Fig. 4). The highest

151   resolution map (Fig. 4C) showed good agreement with the model to confirm the secondary

152   structure and the side chains. Similarly, Fig. 4B also shows reasonable clarity for residue side

153   chains. The slightly lower resolution maps (Fig. 4D, F, G, H) show moderately resolved side chains.

154   The best resolution map obtained using Setting B reported 3.8 Å at 60,000× magnification, but

155   there were some areas where the electron densities of the side chains cannot be clearly recognized;

156   lysine and arginine residues provide examples (Fig. 4, marked with black arrows).

157   While it is still possible to determine larger side chains such as tryptophan, tyrosine and

158   phenylalanine in maps of approximately 4 Å (Fig. 4A, marked with blue arrow), it is difficult to

159   confirm the side chains in maps worse than 4.5 Å resolution (Fig. 4E). In maps with resolutions

160   below 5 Å (Fig. 4H), it is not possible to reliably identify side chains and unstructured loops. At

161   6-8 Å only α-helices were clarified (Rosenthal and Rubinstein, 2015) as demonstrated by the initial

162   model used (Fig. S6).

163

164   **Comparison of data quality in different image conditions**

165   In order to verify the reconstructed maps, the GS-FSC and the map-to-model FSC (MM-FSC)

166   were compared (Fig. 5). The gap between the two FSC values were listed in Table 2. The difference

167   values (Resolution "gap" in Table 2) were averaged in each case, showing (average ± standard

168   error) 0.45±0.075 Å in Setting A and 0.65±0.15 Å in Setting B. These smaller gaps between GS-

169   FSC and MM-FSC of the K2 Summit correlate with the better-quality densities as shown in the

170   maps (Fig. 4, Table 2). This may also come from the result of the superior DQE curve (Fig. S3)

171   and Thon rings of the K2 Summit DED (Fig. S4).

172   The reported resolutions of Setting A between 30,000× and 60,000× magnifications showed a

173   similar parabola shaped curve with Setting B between 40,000× and 100,000× magnifications (Fig.

174   6). The sampling scales at the specimen were nearly identical within these magnification ranges

175   (Fig. 6, Table 2). The result suggests that there is an optimal magnification for high-resolution

176   analysis in each EM setting. The highest resolution was obtained at 50,000× magnification using

177   Setting A, which correspond to the sample scale of 0.75 Å/pixel (Fig. 6). Similarly, the highest

178   resolution with Setting B was obtained at 60,000× magnification, which correspond to the sample

179   scale of 0.95 Å/pixel (Fig. 6). Changing the sample scales on the detector pixel to those on the

180   detector surface, these values are both 0.15 Å/µm (Fig. S7). It further suggests that the highest

181   resolution is performed when the JEOL 200kV TEMs magnify the image at 0.15 Å/µm on the

182   detector surface. The difference of the highest-resolution's nominal magnifications of 50,000× on

183   K2 summit and 60,000× on DE-20 is caused by the difference of the detector positions in each

184   TEM.

185   When calculating Rosenthal-Henderson ("B-factor") plots (Fig. 7), Setting A has a clear

186   advantage over Setting B. The 50,000× Setting A dataset estimates the best B-factor (-161) with

187   40,000× a close second (-172). All Setting A datasets show a non-linear relationship between the

188   points; as particle count drops, resolution decrease accelerates (Fig. 7A). Setting B demonstrates

189   a similar non-linear relationship in datasets where the estimated B-factor is closer to those in

190   Setting A. However, in the two datasets which estimate poor B-factor (approximately -300 or

191   worse) a linear correlation appears (Fig. 7B).

192

Automated acquisition

194   We used β-galactosidase for the sample studied with automation in multi-purpose TEM to

195   demonstrate that usable resolutions (Fig. 8A, B) may be achieved with things other than apoferritin.

196   Further details are listed in Table S1. In roughly the same amount of time – one half an operator

197   day – that we were able to collect ~150 micrographs manually, automation via SerialEM allowed

198   acquisition of ~450. This is without any of the more advanced automatic collection methods such

199   as beam shift acquisition (Cheng et al., 2018). Of these micrographs, 370 were deemed usable

200   post-motion correction and CTF estimation. With automated collection, we achieved a 3.6 Å (Fig.

201   8C) resolution reconstruction of β-galactosidase (Fig. 8). Calculated B-factor (-162) is comparable

202   to those of the apoferritin limited datasets of Setting A 40,000× and 50,000× (Fig. 8D).

203

Discussion

205   After calculation of the Rosenthal-Henderson plots (Fig. 7) for all datasets, we estimated that

206   collecting double or triple the original dataset for the Setting A at 50,000× would achieve 3 Å

207   global resolution. We collected further 126 micrographs to complement the 153 original

208   micrograph movies – this approximately doubled the number of usable particles but was slightly

209   less than double the raw number of micrographs. Using RELION 3.0.8, this did not improve

210   resolution achieved, however moving to a testing build of RELION 3.1, with improved calculation

211   for optical parameters, permitted a 3.0 Å reconstruction with local resolution extending to 2.6 Å

212   when calculated by *blocres* (Heymann, 2001; Heymann and Belnap, 2007). After searching the

213   EMDB (Patwardhan, 2017) this is currently the highest resolution achieved when using a 200KV

214   microscope and (non-autoloader) side-entry cryo-holder system.

215

216   Comparison of EM Settings A and B

217   The first test of a reconstruction is the reported resolution and coincident FSC curve (Fig. S1A,

218   Fig. 5). With this metric, and using the "limited quantity" datasets, Setting A is generally 0.5 Å

219   superior to Setting B, except for 60,000× (Setting A) and 100,000× (Setting B), which can be

220   attributed to the low total number of particles in the narrower field of view of the K2 Summit DED

221   (Fig 2, Table 2). However, if comparing 60,000× (Setting A) with 100,000× (Setting B) (where

222   both have a sampling frequency of 0.62 Å/pixel) then again Setting A becomes superior. While

223   this absolute scale comparison is useful, 100,000× magnification for Setting B has a

224   commensurately higher dose rate and suffers from more instability/drift than 60,000× of Setting

225   A, which is reflected in the Rosenthal-Henderson B-factor estimation (Fig. 7B).

226   The best resolution was achieved at different magnifications in each setting (Figs. 4-6). When

227   we processed the limited micrographs using RELION 3.0, the highest "limited set" resolution of

228   3.3 Å was obtained at 50,000× magnification with Setting A, while the highest resolution of 3.8 Å

229   was obtained at 60,000× magnification with Setting B (Fig. 5, Table 2). Setting A would appear

230   to have optimal conditions at 40,000-50,000×; which magnification recommended would depend

231   on the molecular weight of the sample. Setting B showed little difference between three

232   magnifications (60,000× and 80,000× are detailed herein, the intermediate of the three – 50,000×

233   – is not), although the operator reported that 80,000× was more challenging to acquire than

234   50,000× or 60,000×, while 100,000× was even more so. Setting B provides the ability to collect

235   superior numbers of particles from the same number of micrographs, which may prove

236   advantageous in the case of larger or more heterogenous samples. The use of an Omega filter on

237   Setting B does not appear to either help or hinder processing of data, although it does improve

238   image contrast moderately (Fig. 2) which makes manual data acquisition more user friendly.

239   We hypothesise that the superior performance of Setting A when compared to Setting B is

240   primarily the result of better spherical aberration (Cs: 2 mm) of the JEM-2100F microscope over

241   the JEM-2200FS (Cs: 4.2 mm, which has a worse-than-normal Cs due to modifications necessary

242   for the use of Zernike phase plate hardware) and improved DQE of the K2 Summit DED in the

243   lower frequencies. It would be interesting (and troublesome) to swap the detectors between

244   microscopes and collect further datasets to identify which of these factors has the greater effect.

245

246   **Behaviour of microscope Settings at different magnifications**

247   When the sampling scales on each detector are adjusted respective to the detector surface area, the

248   scale of 50,000× on K2 Summit detector (0.15 Å/μm) of Setting A corresponds to 60,000× on DE-

249   20 detector (0.15 Å/μm) of Setting B. At this point the conditions for the best resolution were

250   coincident between the two acquisition settings (Fig. S7). Similar achievable reconstruction

251   resolution was demonstrated at slightly higher and lower TEM magnifications, with resolution

252   suffering as sampling scale deviated from 0.15 Å/μm at the detector face. This would suggest that

253   there is an optimal magnification for both combinations of microscope and detector at the same

254   detector scale. This should be further investigated across a wider range of microscopes and

255   detectors.

256   In the case of analysing with the same number of particles, it was thought that the resolution

257   improves as the sampling scale becomes smaller. In our processing, this is untrue. This is shown

258   by B-factor plot (Fig. 7) selecting at a given number of particles (e.g.: 10,000 total particles). At

259   higher magnifications, the vibrations and drift that come from the side-entry cryo-holder become

260   more critical and influence the data acquisition in a greater manner. While at lower magnifications,

261   drift and vibrations are less of an issue, and the lower magnification becomes the limiting factor

262   at the detector. Dose also plays a significant role in the quality of acquired data; at higher

263   magnifications the electron dose per $Å^2$ at the sample increases negative effects such as radiation

264   damage, charging, and heating effects resulting in loss of sample mass coupled with large drifts as

265   ice is vaporised. The above phenomenon occurs even though motion correction is performed. We

266   hypothesise that adequate motion correction cannot be performed at a frame processing interval of

267   0.2 s (5 frames per second, fps) at higher dose rates; testing with detectors capable of outputting

268   final micrograph movies of 20fps or greater may prove whether higher dose rates can be offset by

269   higher framerates.

270   While particle polishing acts on a per-particle basis, having good drift correction across initial

271   micrographs results in loss of fewer particles during 2D and 3D classification. In this, patch

272   correction as implemented by MotionCor2 (or the RELION 3 implementation) is superior to

273 whole-frame correction used by the DE-20 manufacturer scripts (Direct Electron, LP) or UNBLUR

274 (Grant and Grigorieff, 2015), although less drift is still preferable. This improved sample stability

275 is one of the advantages of autoloader-equipped microscopes.

276   Although motion correction with dose weighting was performed, there is evidence that at

277 60,000× (Setting A) and 100,000× (Setting B) magnifications that when the dose is optimal for a

278 K2 Summit detector, it is too strong for the sample. Thus, there is increased motion of the sample

279 as the vitrified ice is warmed, combined with faster sample destruction from the electron beam

280 which together cannot be adequately compensated by per-frame motion processing. Because of

281 the nature of recent direct electron detectors, the dose at the sample is determined by the optimal

282 dosage for the detector; to achieve electron counting measurements, this requires a certain

283 minimum dose per detector pixel. At higher magnifications, this can result in extremely high doses

284 on the specimen. Stability dependence is further demonstrated by the power spectra acquired using

285 Pt-Ir film (Fig. S4), where Setting B proves difficult to acquire high quality stable micrographs

286 and which is reflected in the quality of the reconstruction at 100,000×. For Setting A, Thon rings

287 are distinguishable to <2 Å for Setting A (Fig S4A, B), while the last consecutive Thon ring is

288 visible at 2.96 Å (Fig. S4C, D) for Setting B. At lower magnifications, the limiting factor becomes

289 Nyquist frequency and DQE. These are likely the reasons for the "sweet spot" for resolution in our

290 datasets (Fig. 6).

291

292 **Validation of the EM-maps**

293 While the gold-standard FSC is a simple "one number" report of a cryo-EM reconstruction, it is,

294 more precisely, simply a measure of correlation between two independently refined half-maps

295 (Chen et al., 2013; Herzik et al., 2019a; Scheres and Chen, 2012) and thus does not reflect local

296 resolution variability. Map-to-model (MM) FSC is a comparison between a simulated volume

297 generated by a fitted PDB model and either one of the two final half-maps of the GS-FSC or the

298 post-processed (sharpened) full map. It is useful as a quality-of-fit metric for an atomic model,

299 particularly if fitting the model via one half-map, and comparing against the second. The MM-

300 FSC for all Setting A maps is superior to those of the Setting B maps (Fig. 5), although while

301 apoferritin is generally rigid, there is inherent flexibility in protein which will result in minor

302 differences between multiple datasets of the same sample.

303   Local resolution (recently combined with local filtering of a map) provides a finer-grain view
304   of the quality of a reconstruction. The central core of proteins or complexes are generally higher
305   in resolution as they show less flexibility, although this is not always true as some
306   proteins/complexes have highly mobile active sites for substrate binding (Nakane et al., 2018).
307   Apoferritin shows highest resolution at the interaction face between the four bundled helices of
308   each subunit; the contact points of the subunits and the external surfaces show lower resolution.
309   The weakest point of an apoferritin reconstruction is the N-terminal of each subunit, similar to X-
310   ray crystallography where unstructured terminus regions are difficult to resolve.

311   There are many different programs for calculating local resolution; we tested several in the
312   process of this work – although we did not carry out an exhaustive comparison of all the options
313   now available – and finally used the Bsoft (Heymann, 2001; Heymann and Belnap, 2007) *blocres*
314   module similar to recent work by the Lander laboratory (Herzik et al., 2017; Herzik et al., 2019a;
315   Herzik et al., 2019b) as it estimates a range of local resolutions while neither obviously over- or
316   under-estimating, ignoring symmetry or including dramatic resolution transitions.

317   Recent developments (Frenz et al., 2017; Igaev et al., 2019) in molecular dynamics programs
318   have provided methods for fitting atomic models to electron density maps using methods
319   independent of classical crystallographic programs such as COOT (Casanal et al., 2019; Emsley
320   and Cowtan, 2004) or PHENIX (Adams et al., 2010), which have themselves added cryo-EM
321   optimised functions, and which would appear to work well for "mid-to-low" resolution cryo-EM
322   maps which have previously been difficult to interpret with the crystallographic packages. We
323   have not used these here, although are investigating their use for other protein complexes.
324   Ultimately, the human eye remains a good – if potentially biased – method of examining cryo-EM
325   maps. The resolution bounds previously described (Rosenthal and Rubinstein, 2015) for the level
326   of detail which can be expected are a good guide, and it is often immediately apparent whether a
327   map may be the resolution it purports to be.

328

Structural variability of apoferritin

330   The highest resolution map is that acquired at 50,000× on Setting A (Fig. 1A), where ARG63
331   shows two distinct conformations (Fig. 1B, marked with black arrow). This can be used as a further
332   marker of map quality, when density for rotamers becomes distinct. While not as clear as the
333   example of the T20S proteasome (Herzik et al., 2017), conformational shifts upon metal binding

334   would favour increased metal coordination. Further, apoferritin does exhibit minor flexibility when

335   reconstructed without symmetry (at a much-reduced resolution) or with symmetry expansion (Fig.

336   S8).

337   Performing symmetry expansion in RELION 3.0 of 50,000× Setting A and processing with C1

338   symmetry (Fig. S8A) allows some flexibility in the structure (Fig S8B, resolution variations

339   between subunits at the 3-fold symmetry site) to appear; the postprocessing-estimated B-factor

340   value also improves slightly (from -93 to -86) although final estimated resolution of 3.3 Å was

341   unaffected (Fig. S8C). Side chain estimated resolution decreases in an example subunit when

342   reconstructed with symmetry expanded asymmetry (Fig. S8E) compared to when octahedral

343   symmetry is imposed (Fig. S8D), and density for the unstructured loop (Fig. S8E, marked with

344   black arrow) is stronger. A Rosenthal-Henderson plot was not calculated for the symmetry

345   expanded reconstruction, although the RELION 3.1-processed increased dataset (Fig. 1) reported

346   again a slightly higher Rosenthal-Henderson B-factor estimation (-152) than the RELION 3.0-

347   processed 150 micrograph dataset (-161).

348   The behaviour of the datasets with respect to Rosenthal-Henderson plots and estimated B-

349   factor shows a potential relationship between increased field of view and lower estimated B-factor.

350   The lowest magnification of Setting A (30,000×) estimates similar B-factors to Setting B (60,000×

351   and 80,000×), which has a much wider field of view (Fig. 2) although the very high magnifications

352   show similarly poor B-factor estimates (Fig. 7). We attribute these effects to microscope, cryo-

353   holder stability, and radiation damage at the higher magnifications and to increased area for local

354   motions to occur at lower magnifications.

355

Applicability of multi-purpose microscopes in cryo-EM SPA

357   How valid is the use of a multi-purpose TEM for SPA? It will not challenge the most expensive

358   equipment combinations; however, this work demonstrates that even when imposing a limit on

359   data quantity, it is possible to achieve usable resolutions for *de novo* structure determination,

360   provided that other biochemical data is known. For the purpose, it is important to understand the

361   limits created by equipment: which magnifications provide the least drift, most easily optimised

362   dose rate; the detector will influence the rate at which data can be acquired, and potentially usable

363   particles per micrograph. At these resolutions, DQE appears to have less of an impact than was

364   hypothesised.

365   When adding automated acquisition, quantity of data acquired during a similar time period

366   increases, but percentage of good micrographs drops slightly when compared to a skilled operator.

367   Although the potential advantages for users with respect to use of time and work environment

368   cannot be overstated, it remains necessary to maintain regular vigilance of cryogen levels as they

369   are not automatically replenished. The lower symmetry of β-galactosidase offsets the increased

370   quantity of data that was collected using SerialEM automation software (Fig. 8), although in terms

371   of particles picked the two proteins were broadly similar (Table 2, Table S1) and demonstrates that

372   acquisition of lower symmetry protein complexes is viable to achieve usable datasets.

373   There is some utility in comparison of our results to far superior ones of the same complex

374   obtained elsewhere, such as EMD-9599 (Danev et al., 2019), EMD-9865 (Kato et al., 2019) in the

375   electron microscopy data bank (EMDB), as they were acquired using equipment providing the

376   very highest performance possible for cryo-EM SPA. The 1.75 Å map of apoferritin (Wu et al.,

377   2020) from a 200KV microscope further demonstrates the possibilities with increased quantities

378   of data when coupled to optimal grids, sample preparation technique and microscope stability.

379   Although of far greater value is comparing against other datasets, such as the T20S proteasome

380   (Herzik et al., 2017) where ~3 Å (2.8 Å highest local resolution) allowed identification of side

381   chain orientation and tightly bound water molecules on a 200kV microscope, albeit one equipped

382   with an autoloader stage and optimised for SPA. We achieved similar clarity with respect to

383   potential metal-binding sites and residues showing different rotamer states (Fig. 1B, C). While the

384   symmetry of T20S proteasome is not as high (D7, or 14-fold) as apoferritin, the number of particles

385   required for this was an order of magnitude higher than the quantity of data acquired herein,

386   however, exceeding 1,000,000 particles picked and ~80,000 used in the final reconstruction.

387   The recent work demonstrating the application of conventional 200kV hardware to proteins

388   <100kDa (Herzik et al., 2019b) indicates that phase-contrast systems (Danev et al., 2014) are not

389   a requirement for analysis of proteins of that approximate mass. Herzik *et al.* do further discuss

390   the difficulties in processing a 50kDa complex, concluding that phase-contrast may be necessary

391   for these very small complexes, although clarity in 2D class averages may indicate that

392   improvements in image processing solutions would be sufficient. With the improvements

393   demonstrated here when reprocessing a dataset in RELION 3.1 versus RELION 3.0, we agree.

394   For SPA using a multi-purpose TEM, the two primary limiting factors are the ability to collect

395   large volumes of data and maintain sample quality – the latter being something which also affects

396 every TEM, and therefore we consider a null concern for this situation. By achieving a global

397 resolution of 3 Å with a multi-purpose TEM with widely available hardware and limited datasets

398 and comparing two multi-purpose TEM setups, we hope that it will encourage potential users of

399 cryo-EM SPA who do not have access to state-of-the-art facilities.

400

401

Acknowledgements

403 The authors thank Dr. H. Yanagisawa for the gift of the apoferritin test sample, Dr. Jaap Brink

404 (JEOL USA) and Dr. David Mastronarde for help setting up the SerialEM software, and Mr.

405 Yoshihiro Arai (Terabase Inc.) and Mr. Takayuki Owada (Kyodo Printing Co. Ltd.) for renting a

406 Gatan K2 Summit DED. The study was supported by a collaboration program with Terabase Inc.

407

Data availability

409 The cryo-EM reconstructions of all post-processed maps and half maps have been deposited in the

410 EMDB under the accession codes: EMD-30096 (3 Å Setting A 50,000×, RELION 3.1), EMD-

411 30101 (Setting A, 30,000×, RELION 3.0), EMD-30100 (Setting A, 40,000×, RELION 3.0), EMD-

412 30098 (Setting A, 50,000×, RELION 3.0), EMD-30099 (Setting A, 60,000×, RELION 3.0), EMD-

413 30097 (Setting A, 50,000×, RELION 3.0, symmetry expanded), EMD-30103 (Setting B, 40,000×,

414 RELION 3.0), EMD-30105 (Setting B, 60,000×, RELION 3.0), EMD-30106 (Setting B, 80,000×,

415 RELION 3.0), EMD-30107 (Setting B, 100,000×, RELION 3.0), EMD-30095 (Setting A, 40,000×,

416 RELION 3.0, Serial-EM acquisition, β-galactosidase).

417

Author contributions

419 Sample preparation: TK, CS, NT, data acquisition; YK, CS, RNBS, KM; data processing; RNBS,

420 YK, KM, automatic data acquisition: TK, CS, RNBS, KM, draft manuscript; RNBS, YK,

421 manuscript revision; RNBS, YK, CS, KM, conceptualisation; KM, project oversight; KM.

422

Declaration of Interests

424 The authors declare no competing interests.

425

426

427 **Table 1.** Details of TEM Settings A and B

	EM Setting A	EM Setting B
Electron microscope	JEOL JEM-2100F	JEOL JEM-2200FS
Gun type	200KV Schottky	200KV Schottky
Cs (mm)	2.0	4.2
Energy filter	None	Ω-type (15 eV zero-loss)
OLA (μm)	20	20
Detector	Gatan K2 Summit	Direct Electron DE-20
Pixel count	3,708 × 3,836	5,120 × 3,840
Pixel size (μm)	5.0	6.4
Array size (mm)	18 × 19	33 × 25
Mag. Factor	1.5	1.2
Cryo-specimen holder	Gatan 626 LN$_2$	

428

429 **Table 2.** Details of each of eight acquisition conditions

Data collection	EM Setting A				EM Setting B			
TEM magnification	30,000	40,000	50,000	60,000	40,000	60,000	80,000	100,000
Pixel scale (specimen)(Å/pixel)	1.25	0.93	0.75	0.62	1.43	0.95	0.71	0.62
Exposure time (s)	5	5	5	5	5	5	5	3
Dose per second (e$^-$/Å^2/s)	5.35	9.25	12.8	20.8	6.9	8.2	10.0	20.0
Exposure per frame (s)	0.2	0.2	0.2	0.2	0.2	0.2	0.2	0.2
Single particle analysis								
Particles per micrograph (avg.)	1,668	576	329	220	1,697	723	378	320
Acquired micrographs	100	101	153	112	100	150	100	183
Final micrographs	74	70	113	86	74	149	95	97
Final particle count	48,767	24,605	15,680	7,476	36,723	71,528	13,933	8,762
Resolution (Å) GS-FSC (0.143)	4.0	3.4	3.3	3.9	4.5	3.8	3.9	5.1
Validation								

Resolution (Å) MM-FSC (0.5)	4.5	3.6	3.8	4.5	5.3	4.3	4.2	6.1
Resolution "gap"	0.5	0.2	0.5	0.6	0.8	0.5	0.3	1.0
Rosenthal-Henderson (estimated B-factor)	-244	-172	-161	-198	-298	-218	-190	-444

430

431

432   **Figures**

433

A

B

C

HIS65   HIS60   ARG43   MET37   PHE132   LYS146   TYR32   TRP93   TYR34
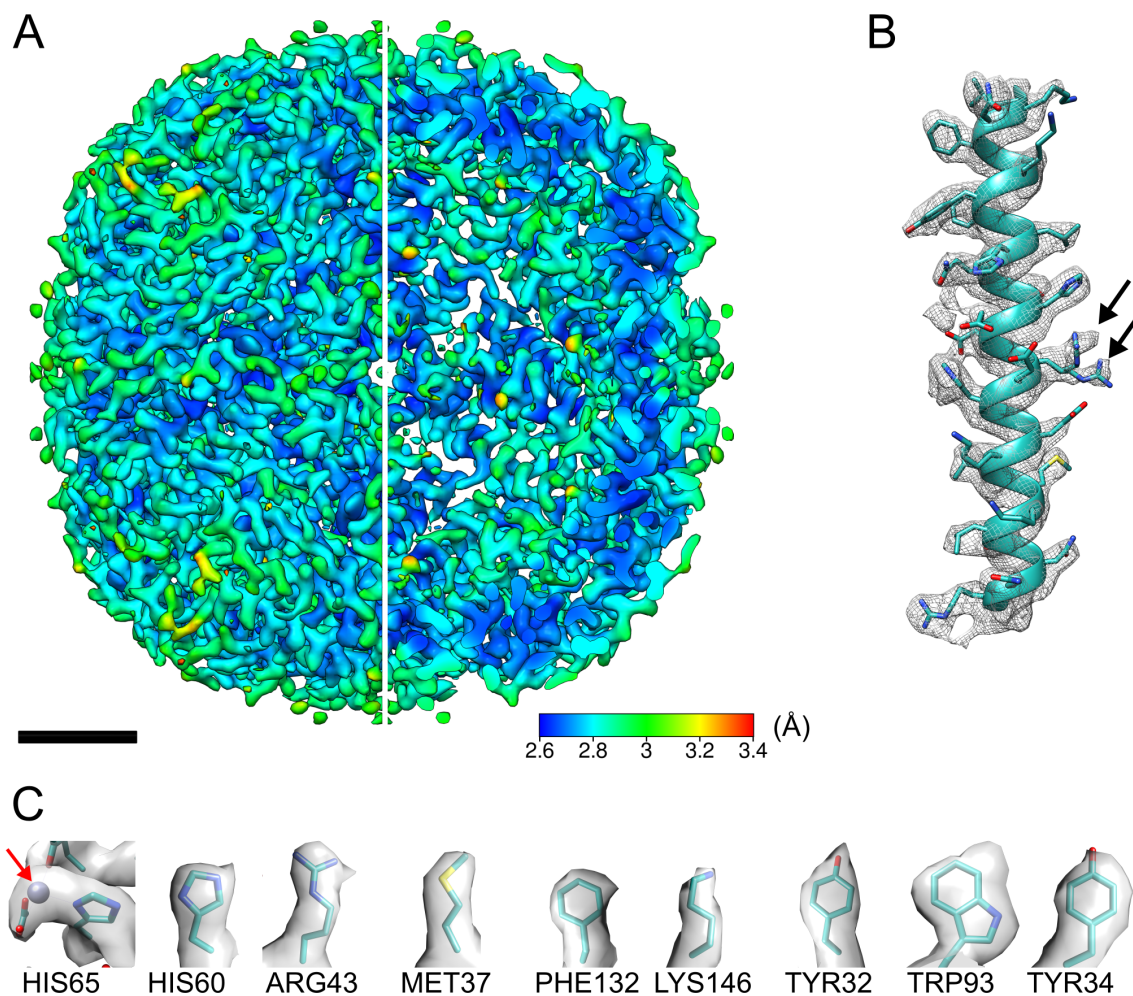
434

435   **Figure 1. 3 Å (global estimated resolution) cryo-EM map of mouse heavy-chain apoferritin.**

436   A) Map coloured by local resolution; one quarter sliced away to allow visualisation of internal

437   density, scale bar 2 nm. B) Representative helix (Leu48-Arg77) from one subunit, with PDB:2CIH

438   fitted. Map is contoured at 3σ. Black arrows show two rotamers of Arg63. C) Nine representative

439   sidechains. Red arrow shows a metal density.

440

441
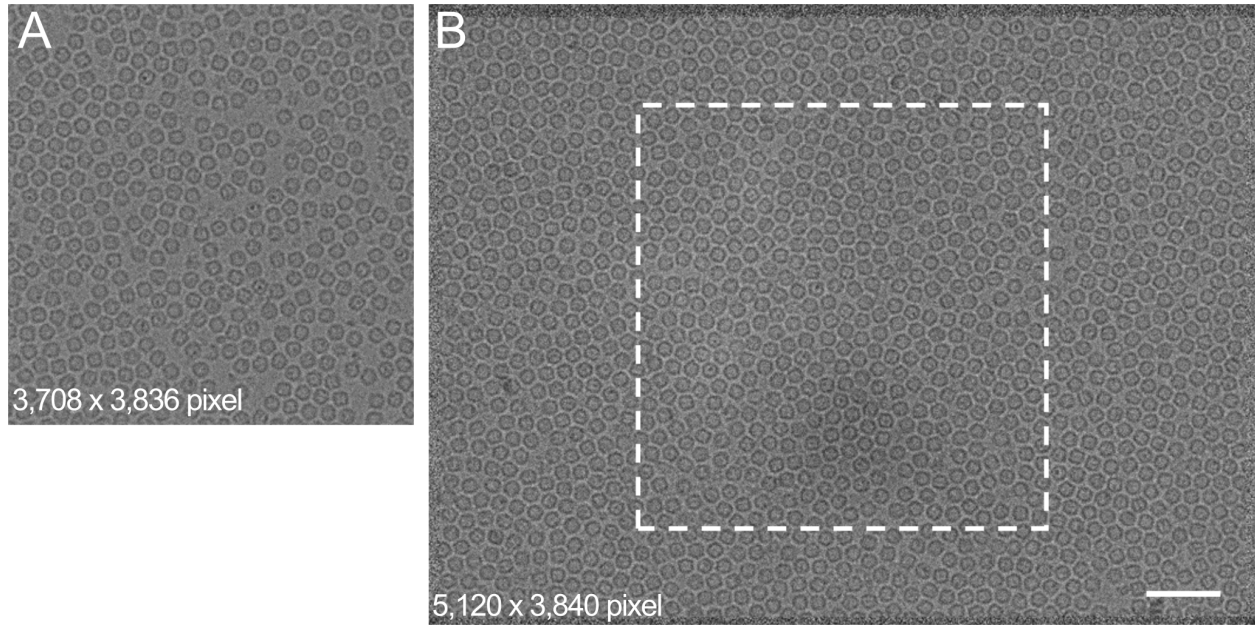
Figure 2. Comparison of micrographs from each microscope and detector combination. Representative micrographs from K2 Summit at 50,000× (A) and from DE-20 at 50,000× (B), each 2.4 μm under-focus. Micrographs scaled to equivalent size, scale bar 50 nm. White dashed box overlaid on image (B) highlights field of view difference between detectors. Micrograph dimensions are included in each figure. As a test sample, purified apoferritin was used. The number of particles included each micrograph were (A) 383, (B) 1,334, respectively. Absolute pixel dimensions are 5.0 μm^2 for K2 Summit DED and 6.4 μm^2 for DE-20 DED.

449
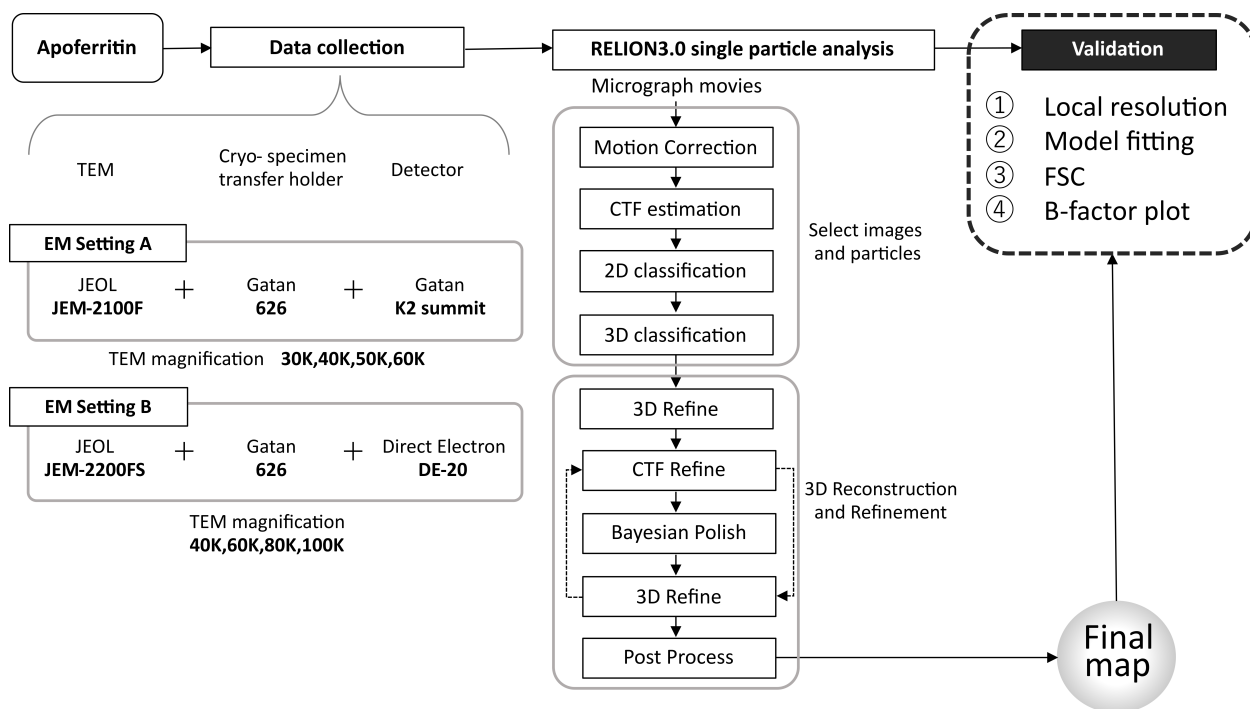
Figure 3. Processing workflow. General schematic of data acquisition and processing is described. Two electron microscope setups were used: JEM-2100F + Gatan 626 + Gatan K2 Summit detector (Setting A) and JEM-2200FS + Gatan 626 + Direct Electron DE-20 detector (Setting B). Each data set was processed using RELION 3.0 and evaluated with procedures shown in the figure. Further specifics of the equipment can be found in Table 1.

457
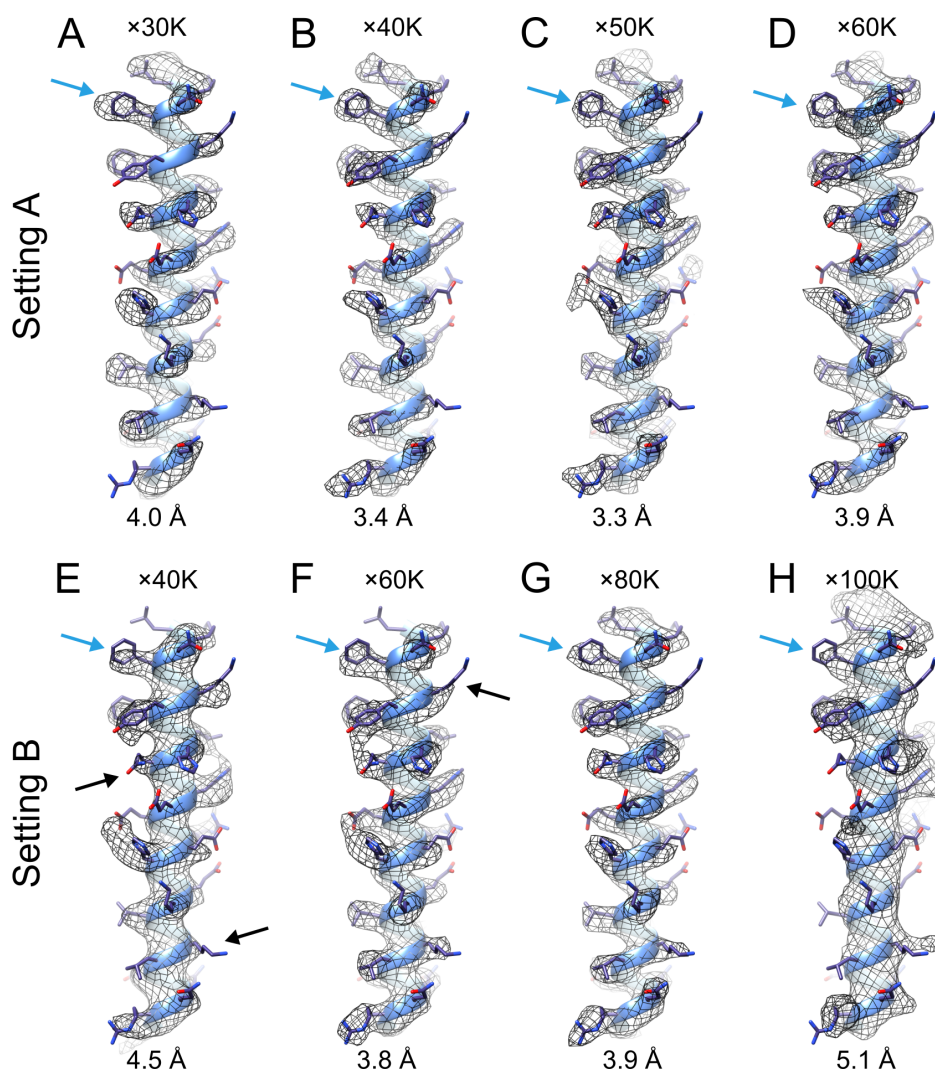
Figure 4. Density comparison between eight reconstruction segments. A representative α-helix (Leu48-Arg77) was extracted from each cryo-EM map and the corresponding atomic model (PDB ID: 2CIH) was fitted to each map. The maps in the top panel are reconstruct from datasets acquired by Setting A, at magnifications of ×30K (A), ×40K (B), ×50K (C), and ×60K (D). The map in a bottom panel are reconstructed from data sets acquired by Setting B, at magnifications of ×40K (E), ×60K (F), ×80K (G), and ×100K (H). The obtained resolutions are labelled in each map. Leu69 is indicated by blue arrows. Black arrows highlight exemplar sidechains which may present difficulties in identification.

466

467
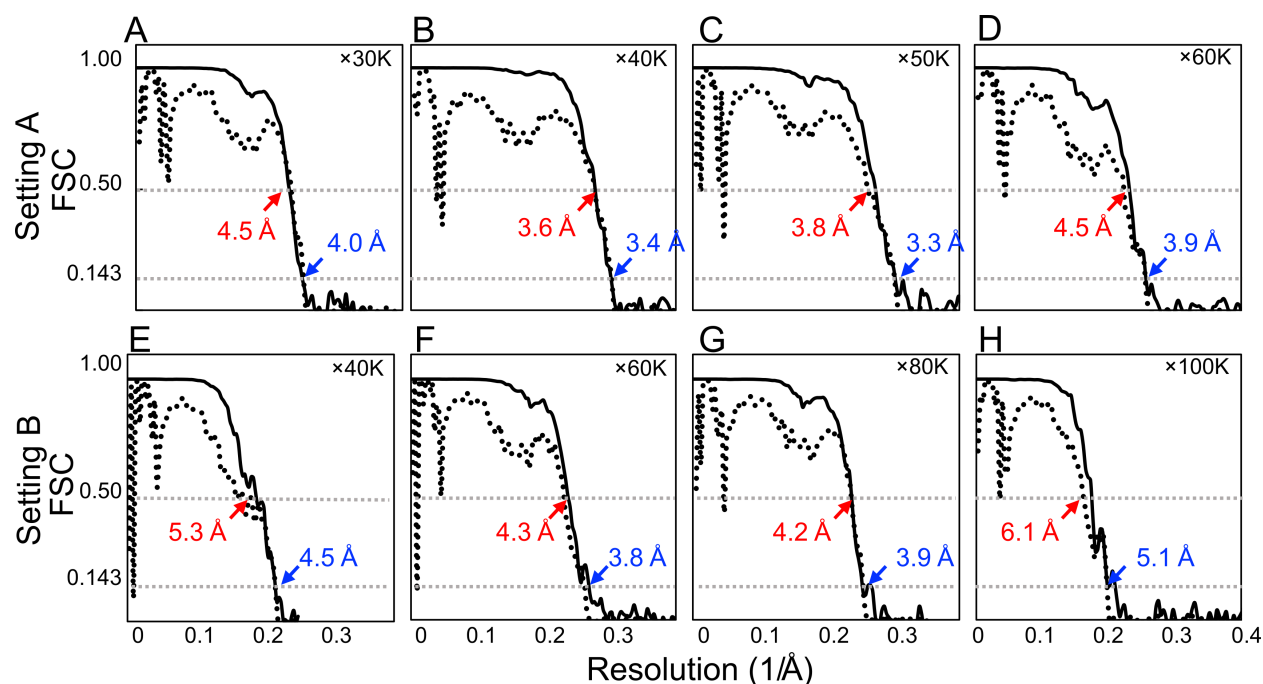
Figure 5. GS-FSC and MM-FSC plots of all reconstructions. GS-FSC (solid lines) was calculated from independent half maps, and the resolutions was estimated at 0.143 cut-off (blue labels). MM-FSC (dashed lines) were calculated between 3D reconstructions and maps calculated from the PDB model (2CIH), and the resolution was estimated at 0.5 cut-off (red labels). The experimental conditions are ×30K (A), ×40K (B), ×50K (C), and ×60K (D) magnifications using Setting A, and ×40K (E), ×60K (F), ×80K (G), and ×100K (H) magnifications using Setting B.

474
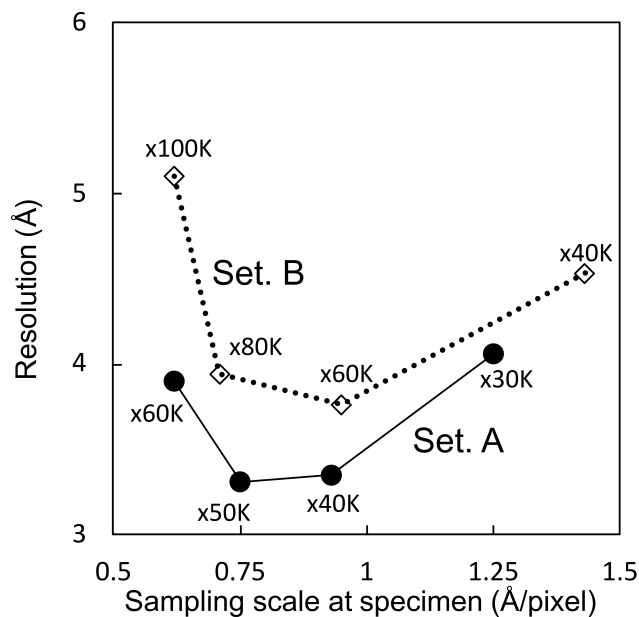
Figure 6. Plot of the achieved resolution of each magnification with different EM settings. The achieved resolutions of Setting A (solid dots) and Setting B (empty diamonds) at each magnification are connected by solid and dot lines, respectively. X-axis shows the sampling scale at the specimen.
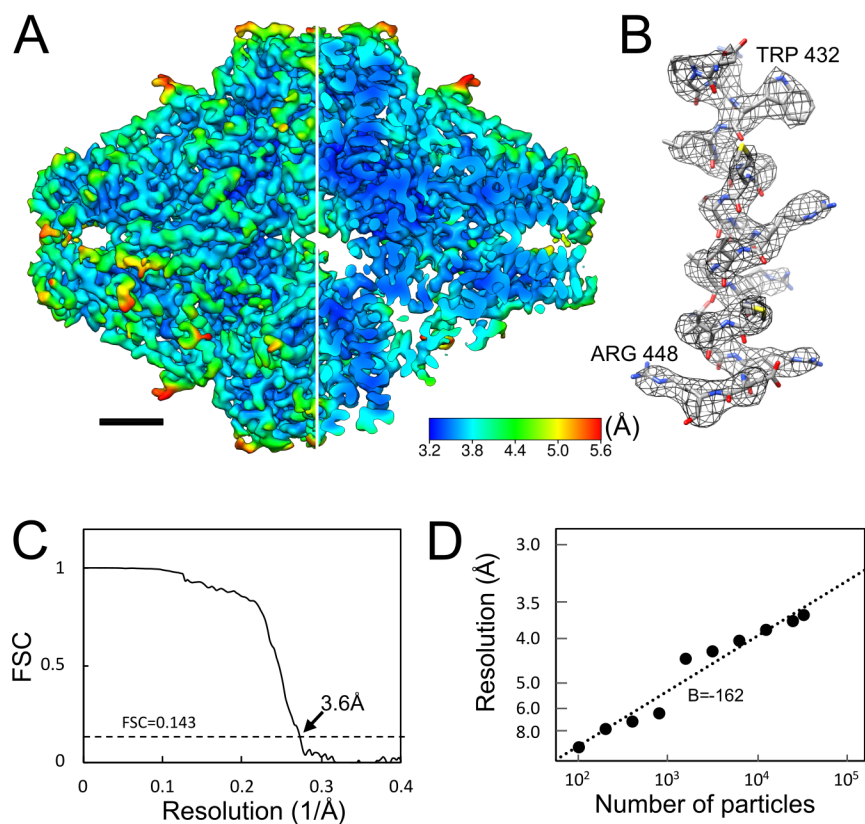
481
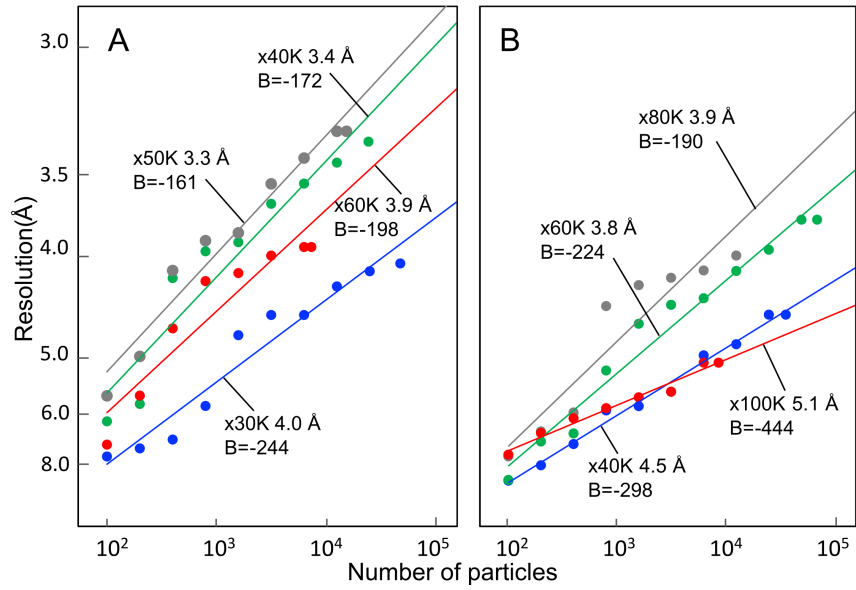
Figure 7. B-factor plots of all reconstructions. The points were calculated by *bfactor_plot.py* in RELION 3.0 at different magnifications. B-factor values are estimated from the fitted slopes. (A) Setting A and (B) Setting B. Magnifications are labelled appropriately.

482

483

484

485

486

Figure 8. β-galactosidase reconstruction from Setting A using SerialEM automated software. Data was acquired in the same time period as other datasets, except via automation rather than manual operation. A) 3.6 Å (global estimated resolution) reconstruction coloured by local resolution, one quarter sliced away to allow visualisation of internal density. Map is contoured at 5σ. B) Representative helix (residues ASP429-ARG448) showing side-chain clarity. C) FSC curve. D) Rosenthal-Henderson plot, estimating B-factor. Estimated B-factor is dependent on whether extremely low-particle-count reconstructions are included, which influences the overall B-factor estimate.

495

496

References

Adams, P.D., Afonine, P.V., Bunkoczi, G., Chen, V.B., Davis, I.W., Echols, N., Headd, J.J., Hung, L.W., Kapral, G.J., Grosse-Kunstleve, R.W., McCoy, A.J., Moriarty, N.W., Oeffner, R., Read, R.J., Richardson, D.C., Richardson, J.S., Terwilliger, T.C., Zwart, P.H., 2010. PHENIX: a comprehensive Python-based system for macromolecular structure solution. Acta Crystallogr D Biol Crystallogr 66, 213-221.

Allen, L.J., D'Alfonso, A.J., Freitag, B., Klenov, D.O., 2012. Chemical mapping at atomic resolution using energy-dispersive x-ray spectroscopy. Mrs Bull 37, 47-52.

Bammes, B.E., Rochat, R.H., Jakana, J., Chen, D.-H., Chiu, W., 2012. Direct electron detection yields cryo-EM reconstructions at resolutions beyond 3/4 Nyquist frequency. Journal of Structural Biology 177, 589-601.

Bartesaghi, A., Merk, A., Banerjee, S., Matthies, D., Wu, X., Milne, J.L., Subramaniam, S., 2015. 2.2 Å resolution cryo-EM structure of beta-galactosidase in complex with a cell-permeant inhibitor. Science 348, 1147-1151.

Baumeister, W., 2002. Electron tomography: towards visualizing the molecular organization of the cytoplasm. Curr Opin Struct Biol 12, 679-684.

Bhella, D., 2019. Cryo-electron microscopy: an introduction to the technique, and considerations when working to establish a national facility. Biophys Rev 11, 515-519.

Carragher, B., Kisseberth, N., Kriegman, D., Milligan, R.A., Potter, C.S., Pulokas, J., Reilein, A., 2000. Leginon: an automated system for acquisition of images from vitreous ice specimens. J Struct Biol 132, 33-45.

Casanal, A., Lohkamp, B., Emsley, P., 2019. Current Developments in Coot for Macromolecular Model Building of Electron Cryo-microscopy and Crystallographic Data. Protein Sci.

Chen, S., McMullan, G., Faruqi, A.R., Murshudov, G.N., Short, J.M., Scheres, S.H., Henderson, R., 2013. High-resolution noise substitution to measure overfitting and validate resolution in 3D structure determination by single particle electron cryomicroscopy. Ultramicroscopy 135, 24-35.

Cheng, A., Eng, E.T., Alink, L., Rice, W.J., Jordan, K.D., Kim, L.Y., Potter, C.S., Carragher, B., 2018. High resolution single particle cryo-electron microscopy using beam-image shift. J Struct Biol 204, 270-275.

527   Cressey, D., Callaway, E., 2017. Cryo-electron microscopy wins chemistry Nobel. Nature 550,
528   167.

529   Crewe, A.V., Wall, J., Langmore, J., 1970. Visibility of single atoms. Science 168, 1338-1340.

530   Danev, R., Yanagisawa, H., Kikkawa, M., 2019. Cryo-Electron Microscopy Methodology: Current
531   Aspects and Future Directions. Trends Biochem Sci 44, 837-848.

532   Egerton, R.F., 2009. Electron energy-loss spectroscopy in the TEM. Rep Prog Phys 72.

533   Emsley, P., Cowtan, K., 2004. Coot: model-building tools for molecular graphics. Acta Crystallogr
534   D Biol Crystallogr 60, 2126-2132.

535   Faruqi, A.R., McMullan, G., 2018. Direct imaging detectors for electron microscopy. Nuclear
536   Instruments and Methods in Physics Research Section A: Accelerators, Spectrometers,
537   Detectors and Associated Equipment 878, 180-190.

538   Frenz, B., Walls, A.C., Egelman, E.H., Veesler, D., DiMaio, F., 2017. RosettaES: a sampling
539   strategy enabling automated interpretation of difficult cryo-EM maps. Nat. Methods 14,
540   797-+.

541   Grant, T., Grigorieff, N., 2015. Measuring the optimal exposure for single particle cryo-EM using
542   a 2.6 A reconstruction of rotavirus VP6. Elife 4, e06980.

543   Grant, T., Rohou, A., Grigorieff, N., 2018. *cis*TEM, user-friendly software for single-particle
544   image processing. eLife 7.

545   Hamaguchi, T., Maki-Yonekura, S., Naitow, H., Matsuura, Y., Ishikawa, T., Yonekura, K., 2019.
546   A new cryo-EM system for single particle analysis. J Struct Biol 207, 40-48.

547   Herzik, M.A., Jr., Wu, M., Lander, G.C., 2017. Achieving better-than-3-A resolution by single-
548   particle cryo-EM at 200 keV. Nat Methods 14, 1075-1078.

549   Herzik, M.A., Jr., Fraser, J.S., Lander, G.C., 2019a. A Multi-model Approach to Assessing Local
550   and Global Cryo-EM Map Quality. Structure 27, 344-358 e343.

551   Herzik, M.A., Jr., Wu, M., Lander, G.C., 2019b. High-resolution structure determination of sub-
552   100 kDa complexes using conventional cryo-EM. Nat Commun 10, 1032.

553   Heymann, J.B., 2001. Bsoft: image and molecular processing in electron microscopy. J Struct Biol
554   133, 156-169.

555   Heymann, J.B., Belnap, D.M., 2007. Bsoft: image processing and molecular modeling for electron
556   microscopy. J Struct Biol 157, 3-18.

557   Igaev, M., Kutzner, C., Bock, L.V., Vaiana, A.C., Grubmuller, H., 2019. Automated cryo-EM
558   structure refinement using correlation-driven molecular dynamics. Elife 8.

559   Iudin, A., Korir, P.K., Salavert-Torres, J., Kleywegt, G.J., Patwardhan, A., 2016. EMPIAR: a
560   public archive for raw electron microscopy image data. Nat Methods 13, 387-388.

561   Kato, T., Makino, F., Nakane, T., Terahara, N., Kaneko, T., Shimizu, Y., Motoki, S., Ishikawa, I.,
562   Yonekura, K., Namba, K., 2019. CryoTEM with a Cold Field Emission Gun That Moves
563   Structural Biology into a New Stage. Microscopy and Microanalysis 25, 998-999.

564   Kimanius, D., Forsberg, B.O., Scheres, S.H., Lindahl, E., 2016. Accelerated cryo-EM structure
565   determination with parallelisation using GPUs in RELION-2. eLife 5.

566   Knapek, E., Lefranc, G., Heide, H.G., Dietrich, I., 1982. Electron microscopical results on
567   cryoprotection of organic materials obtained with cold stages. Ultramicroscopy 10, 105-
568   110.

569   Kuijper, M., van Hoften, G., Janssen, B., Geurink, R., De Carlo, S., Vos, M., van Duinen, G., van
570   Haeringen, B., Storms, M., 2015. FEI's direct electron detector developments: Embarking
571   on a revolution in cryo-TEM. Journal of Structural Biology 192, 179-187.

572   Mastronarde, D.N., 2005. Automated electron microscope tomography using robust prediction of
573   specimen movements. Journal of Structural Biology 152, 36-51.

574   McMullan, G., Faruqi, A.R., Henderson, R., 2016. Direct Electron Detectors. Methods Enzymol
575   579, 1-17.

576   Morishita, S., Yamasaki, J., Tanaka, N., 2013. Measurement of spatial coherence of electron beams
577   by using a small selected-area aperture. Ultramicroscopy 129, 10-17.

578   Murata, K., Wolf, M., 2018. Cryo-electron microscopy for structural analysis of dynamic
579   biological macromolecules. Biochim. Biophys. Acta 1862, 324-334.

580   Nakane, T., Kimanius, D., Lindahl, E., Scheres, S.H.W., 2018. Characterisation of molecular
581   motions in cryo-EM single-particle data by multi-body refinement in RELION. eLife 7.

582   Nannenga, B.L., Gonen, T., 2019. The cryo-EM method microcrystal electron diffraction
583   (MicroED). Nature Methods 16, 369-379.

584   Patwardhan, A., 2017. Trends in the Electron Microscopy Data Bank (EMDB). Acta Crystallogr
585   D 73, 503-508.

586   Punjani, A., Rubinstein, J.L., Fleet, D.J., Brubaker, M.A., 2017. cryoSPARC: algorithms for rapid
587   unsupervised cryo-EM structure determination. Nat Methods 14, 290-296.

588   Richter, G.W., 1959. Internal Structure of Apoferritin as Revealed by the "Negative Staining
589   Technique.". J Biophys Biochem Cytol 6, 531-534.

590   Rosenthal, P.B., Rubinstein, J.L., 2015. Validating maps from single particle electron
591   cryomicroscopy. Curr. Opin. Struct. Biol. 34, 135-144.

592   Ruskin, R.S., Yu, Z.H., Grigorieff, N., 2013. Quantitative characterization of electron detectors
593   for transmission electron microscopy. Journal of Structural Biology 184, 385-393.

594   Russo, C.J., Passmore, L.A., 2014. Electron microscopy: Ultrastable gold substrates for electron
595   cryomicroscopy. Science 346, 1377-1380.

596   Scheres, S.H., Chen, S., 2012. Prevention of overfitting in cryo-EM structure determination. Nat.
597   Methods 9, 853-854.

598   Toussaint, L., Bertrand, L., Hue, L., Crichton, R.R., Declercq, J.P., 2007. High-resolution X-ray
599   structures of human apoferritin H-chain mutants correlated with their activity and metal-
600   binding sites. J Mol Biol 365, 440-452.

601   Wu, M., Lander, G.C., Herzik Jr, M.A., 2020. Sub-2 Angstrom resolution structure determination
602   using single-particle cryo-EM at 200 keV. Journal of Structural Biology: X, 100020.

603   Zheng, S.Q., Palovcak, E., Armache, J.P., Verba, K.A., Cheng, Y., Agard, D.A., 2017.
604   MotionCor2: anisotropic correction of beam-induced motion for improved cryo-electron
605   microscopy. Nat Methods 14, 331-332.

606   Zivanov, J., Nakane, T., Forsberg, B.O., Kimanius, D., Hagen, W.J., Lindahl, E., Scheres, S.H.,
607   2018. New tools for automated high-resolution cryo-EM structure determination in
608   RELION-3. Elife 7.

609

610

611   **Methods**

612

613   **Cryo-electron microscopy**

614   High-symmetry (24-fold/octahedral) heavy-chain apoferritin was used as a test specimen, which

615   was the generous gift of Dr. H. Yanagisawa, University of Tokyo. β-galactosidase (SIGMA-

616   ALDRICH, St. Louis, MO) was purified by gel filtration on a Superdex-200 size-exclusion

617   chromatography column connected to an ÄKTA FPLC apparatus (GE Healthcare Bio-Sciences,

618   Piscataway, NJ) with an elution buffer comprised of 25 mM Tris (pH 8), 50 mM NaCl, 2 mM

619      $MgCl_2$ and 1mM TCEP. An aliquot of sample solution was applied to standard molybdenum

620   Quantifoil grids R1.2/1.3 (Quantifoil Micro Tools GmbH) and vitrified by rapid plunging in

621   liquefied ethane using a Vitrobot Mark IV (Thermo Fisher Scientific) at 95% humidity and 4 °C.

622   The frozen grid was mounted on a Gatan 626 cryo-transfer specimen holder at liquid nitrogen

623   temperature and loaded into either a JEM2100F microscope (JEOL) equipped with a K2 Summit

624   DED (Gatan) (Setting A) or a JEM2200FS microscope (JEOL) equipped with a DE-20 DED

625   (Direct Electron LP) (Setting B). Magnifications were varied and are detailed in Table 2. Both

626   microscopes were operated with thermal Schottky electron source at 200kV. In the case of

627   JEM2200FS, an Omega-type energy filter was used with a slit width of 15 eV. Spherical

628   aberrations of each pole piece were 2.0 mm (JEM2100F) and 4.2 mm (JEM2200FS). The

629   illumination conditions were optimized for K2 Summit counting mode (8 e⁻/pixel/sec on detector)

630   and maintained through DE-20 acquisition for comparison purposes via low dose acquisition,

631   although at 80,000× and 100,000× magnification the dose rate for DE-20 acquired data was

632   considered very high. Further details can be found in Table 2. Movies were collected over a

633   minimum of 3 seconds at 5 fps (frames per second) in both detectors.

634

635   **Image processing**

636   Movies were motion-corrected using the MotionCor2 algorithm (Zheng et al., 2017) as

637   implemented in RELION 3 (Zivanov et al., 2018) using dose-weighting and patch correction with

638   5x5 grid for K2 Summit DED and 5x3 grid for the DE-20 DED. CTF was estimated by CTFFIND4

639   (4.1.10) (Rohou and Grigorieff, 2015). Particles were picked by either a) using the RELION 3

640   LoG-based (Laplacian of Gaussian) auto picker (Zivanov et al., 2018) or b) manually picking 100-

641   200 particles, as the shape of apoferritin means that more particles are not needed for autopicking.

642   The box size was determined so that one edge was between 180 to 240 Å, and extracted particles

643   were 2D-classified. Good classes were used as a reference for a second round of auto picking. The

644   extracted particles were sorted against the autopicking references and the worst particles discarded,

645   after which they were subjected to 3D classification using a map generated *ab initio* using the

646   cisTEM (Grant et al., 2018) algorithm as a reference, with octahedral symmetry (Fig. S5). The

647   best class(es) were selected, and a map was refined via Refine3D followed by postprocessing. For

648   further optimization, CTF refinement and Bayesian polishing were performed on the obtained

649   input particles, and Refine3D was performed again to obtain the final map. Local resolution was

650   calculated using *blocres* (with default settings but defining symmetry) from the Bsoft package

651   (Heymann and Belnap, 2007). The procedure is summarized in Fig. 3. Processing in RELION 3.1

652   proceeded in a similar fashion except for the particle sorting step, which has been removed in the

653   current testing versions of RELION 3.1. Visualisation of 2D and 3D images were carried out using

654   RELION (Zivanov et al., 2018), Fiji (Schindelin et al., 2012) or UCSF Chimera 1.11.2 (Pettersen

655   et al., 2004) depending on dimensionality.

656

657   **Model fitting and map validation**

658   An x-ray crystallographic-derived atomic model (PDBID: 2CIH) was fitted to the obtained eight

659   maps using the "fit in map" function in UCSF Chimera (1.11.2) (Pettersen et al. 2004). The maps

660   were segmented using SEGGER (v1.4.9) (Pintilie et al., 2010) and an α-helix corresponding to

661   residues 48-77 was visualized for each map. FSC curves of each of the data sets were calculated.

662   The correlation between half-maps (GS-FSC) (Chen et al., 2013) was estimated by 0.143 cut-off

663   (Rosenthal and Henderson, 2003), and the correlation between map and atomic model (PDB ID:

664   2CIH) (MM-FSC) was calculated with 0.5 cut-off. The PDB-based atomic model map was

665   generated using UCSF Chimera's "*molmap*" function (Pettersen et al., 2004) at the GS-FSC

666   resolution of each reconstructed map. The CTFFIND estimated resolution was assessed by analysis

667   of the logfiles generated by CTFFIND4 (Rohou and Grigorieff, 2015). B-factor plots were

668   calculated by running an appropriately modified copy of RELION's script, *bfactor_plot.py*. The

669   script randomly selects subsets of particles from each data set and executes Refine3D and

670   Postprocess steps. Plotting the natural logarithm of each particle subset against the inverse of the

671   squared resolution for each refinement allows estimation of particle and dataset quality by

672   correlation of a linear fit (Zivanov et al., 2018).

673

674   **Assessment of TEM's performance**

675   DQE curves were measured using the shadow of a beam stopper. The obtained data was processed

676   by FindDQE (Ruskin et al., 2013). Thon rings are compared with two TEM settings by using FFT

677   of Pt-Ir micrograms with the same data acquisition condition. Radial profiles were generated by

678   Gatan Microscopy Suite 3 (Gatan, Inc.).

679

680   **References: materials and methods**

681   Grant, T., Rohou, A., Grigorieff, N., 2018. *cis*TEM, user-friendly software for single-particle
682   image processing. eLife 7.
683   Heymann, J.B., Belnap, D.M., 2007. Bsoft: image processing and molecular modeling for electron
684   microscopy. J Struct Biol 157, 3-18.
685   Pettersen, E.F., Goddard, T.D., Huang, C.C., Couch, G.S., Greenblatt, D.M., Meng, E.C., Ferrin,
686   T.E., 2004. UCSF Chimera--a visualization system for exploratory research and analysis.
687   J. Comput. Chem. 25, 1605-1612.
688   Pintilie, G.D., Zhang, J., Goddard, T.D., Chiu, W., Gossard, D.C., 2010. Quantitative analysis of
689   cryo-EM density map segmentation by watershed and scale-space filtering, and fitting of
690   structures by alignment to regions. J Struct Biol 170, 427-438.
691   Rohou, A., Grigorieff, N., 2015. CTFFIND4: Fast and accurate defocus estimation from electron
692   micrographs. J. Struct. Biol. 192, 216-221.
693   Rosenthal, P.B., Henderson, R., 2003. Optimal determination of particle orientation, absolute hand,
694   and contrast loss in single-particle electron cryomicroscopy. J Mol Biol 333, 721-745.
695   Ruskin, R.S., Yu, Z.H., Grigorieff, N., 2013. Quantitative characterization of electron detectors
696   for transmission electron microscopy. Journal of Structural Biology 184, 385-393.
697   Schindelin, J., Arganda-Carreras, I., Frise, E., Kaynig, V., Longair, M., Pietzsch, T., Preibisch, S.,
698   Rueden, C., Saalfeld, S., Schmid, B., Tinevez, J.-Y., White, D.J., Hartenstein, V., Eliceiri,
699   K., Tomancak, P., Cardona, A., 2012. Fiji: an open-source platform for biological-image
700   analysis. Nat. Methods 9, 676.
701   Zheng, S.Q., Palovcak, E., Armache, J.P., Verba, K.A., Cheng, Y., Agard, D.A., 2017.
702   MotionCor2: anisotropic correction of beam-induced motion for improved cryo-electron
703   microscopy. Nat Methods 14, 331-332.
704   Zivanov, J., Nakane, T., Forsberg, B.O., Kimanius, D., Hagen, W.J., Lindahl, E., Scheres, S.H.,
705   2018. New tools for automated high-resolution cryo-EM structure determination in
706   RELION-3. Elife 7.
707

708   **Supplementary information**

709

710   **Table S1.** Details of acquisition conditions for β-galactosidase via SerialEM.

Microscope	Setting A
TEM magnification	40,000×
Pixel scale (specimen)(Å/pixel)	0.93
Exposure time (s)	5
Dose per second (e$^-$/Å^2/s)	10.6
Exposure per frame	0.2
Micrographs per hour (SerialEM)	~75
Data collection time (h)	6
Total micrographs collected	451
Pause for refilling LN$_2$	2 (10 min. each)
Single particle analysis	
Particles per micrograph (avg.)	381
Number of micrographs used	370
Final particle count	50,523
Resolution (Å) GS-FSC (0.143)	3.6
Validation	
Resolution (Å) MM-FSC (0.5)	4.2
Rosenthal-Henderson (estimated B-factor)	-162

711

712

713
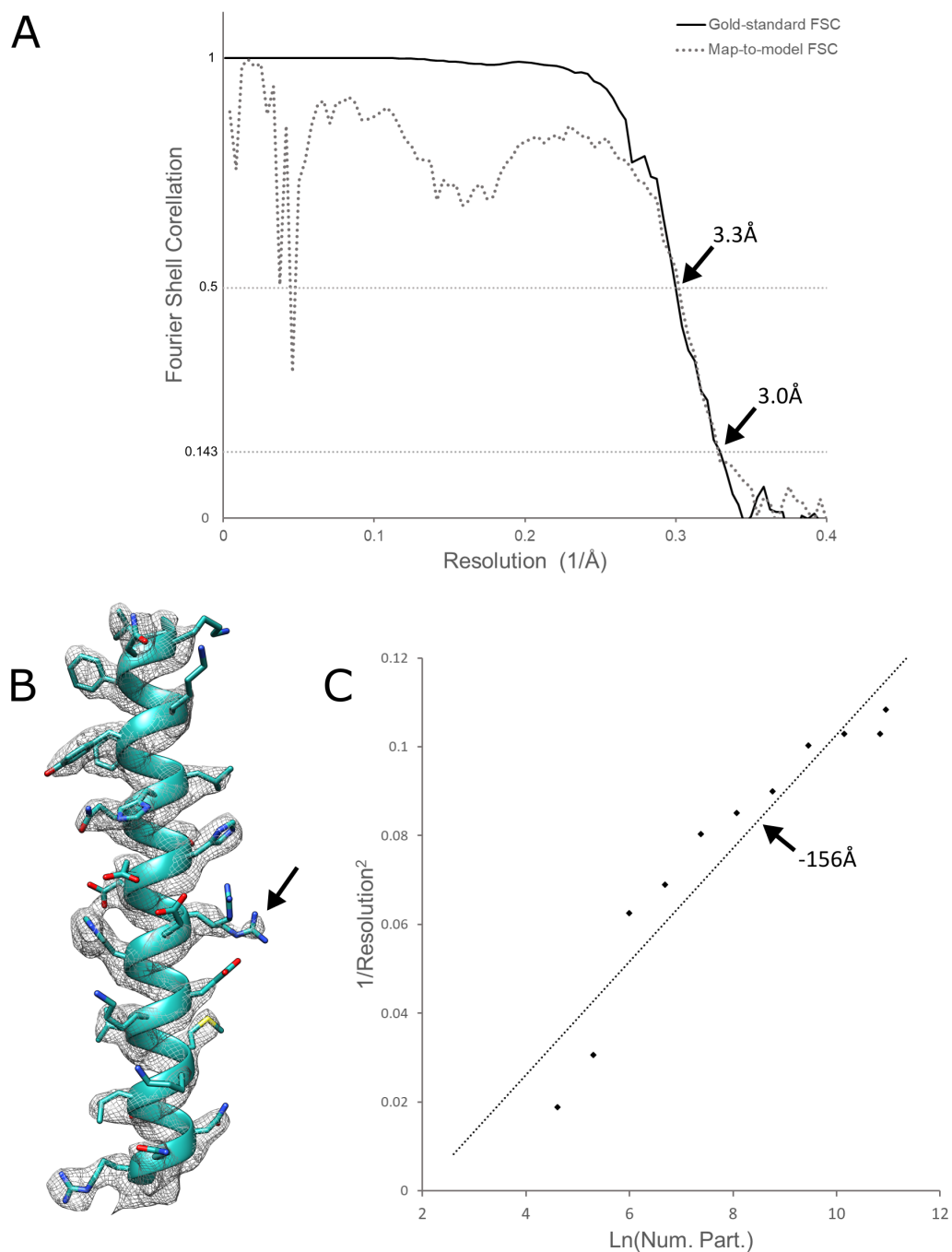
Figure S1. Additional data for Fig. 1. A) Gold-standard FSC (black line) and Map-to-model FSC (dashed line) for 3 Å (global estimate) apoferritin reconstruction. B) The helix from Fig. 1B, contoured at 5σ rather than 3σ (Fig. 1B), permitting visualisation of the loss of one of the ARG63 rotamer densities, indicating that it may be a less favourable conformation. C) Rosenthal-Henderson plot, estimating B-factor to be -162.
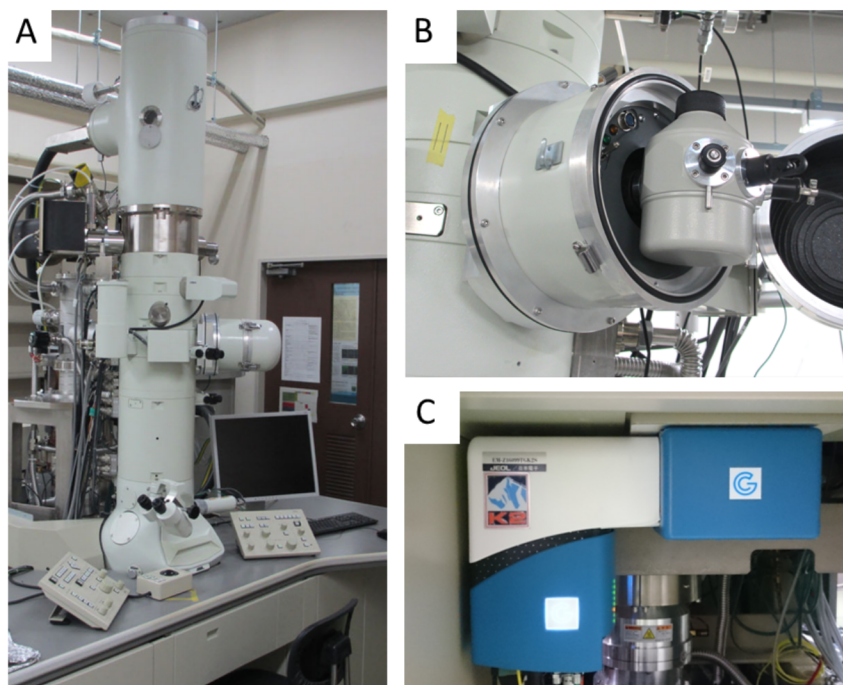
719

720 **Figure S2. One of two electron microscope settings.** Gatan K2 Summit DED (C) is mounted on

721 JEM-2100F microscope (A). Gatan 626 cryo-specimen holder is used to sustain the frozen grid at

722 liquid Nitrogen temperature (B). The second electron microscope setting has been detailed

723 previously (Murata and Wolf, 2018).

724
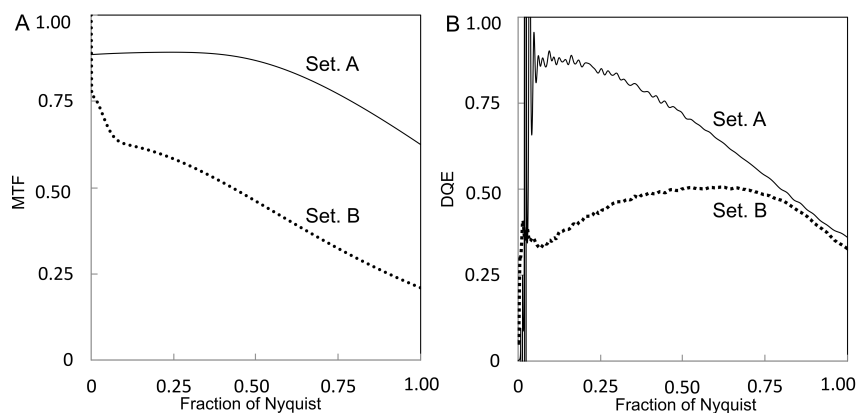
725

726 **Figure S3. Modulation transfer function (MTF) and Detective quantum efficiency (DQE)**

727 **curves in EM settings A and B.** A) MTF curves for each setting, B) calculated DQE for each

728 setting. DQE curves are estimated with a beam stopper using FindDQE software (Ruskin et al.,

729 2013).

730
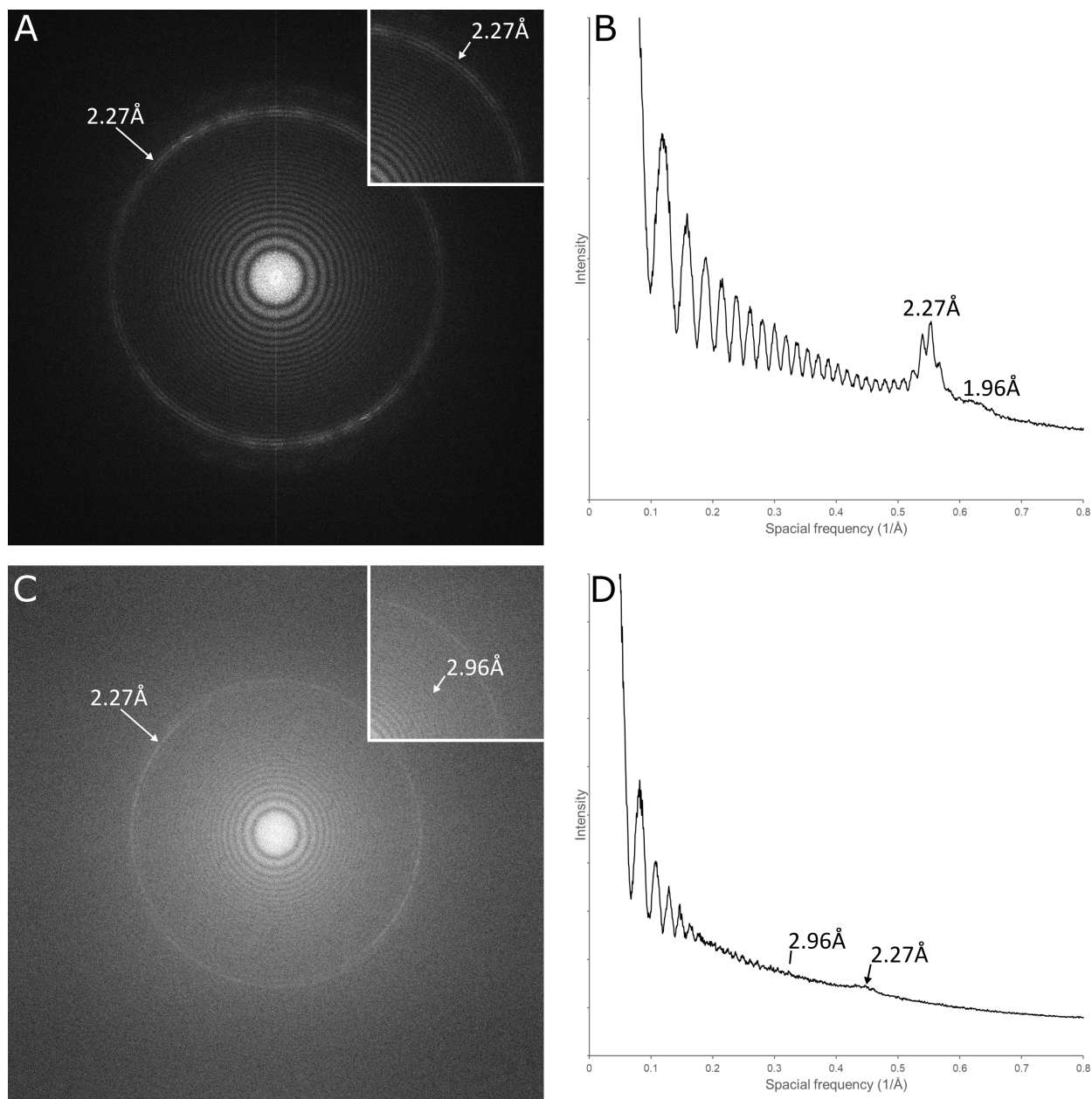
Figure S4. Thons rings of FFT images of Pt-Ir film. Micrographs of Pt-Ir film were acquired by Setting A and B at 100,000×, 0.5μm defocus, and the power spectrum were generated by FFT. A) Setting A power spectrum, B) Plot of rotationally averaged radial profile of (A), C) Setting B power spectrum, D) Plot of rotationally averaged radial profile of (C). With Setting A, Thon rings are clearly distinguishable to the diffraction ring; with Setting B, difficulties in maintaining stability have caused a slight drift in defocus and minor astigmatism resulting in blurring of the rotationally averaged profile.

738
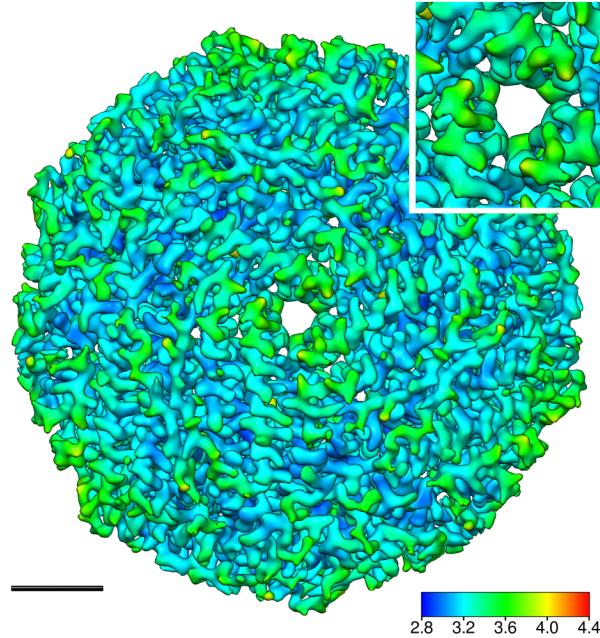
Figure S5. The best resolution map of apoferritin at 3.3 Å generated by Setting A. It was achieved at 50,000× magnification. The local resolution was coloured from 2.8 to 3.6 Å resolution. Surface depicted at 4σ. Breakout focussed on 3-fold symmetry axis, where estimated local resolution for each subunit is identical. Scale bar equals 2 nm.


743
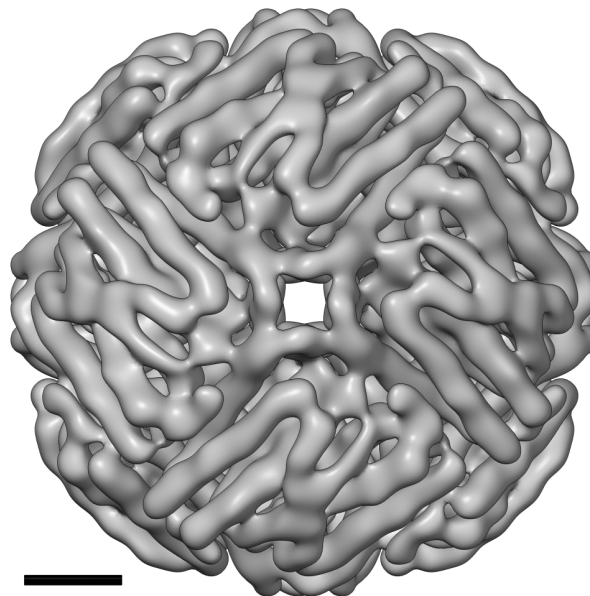
Figure S6. A representative *ab initio* 8 Å initial model of apoferritin. The map was generated with *cis*TEM (Grant et al., 2018). Scale bar equals 2 nm.
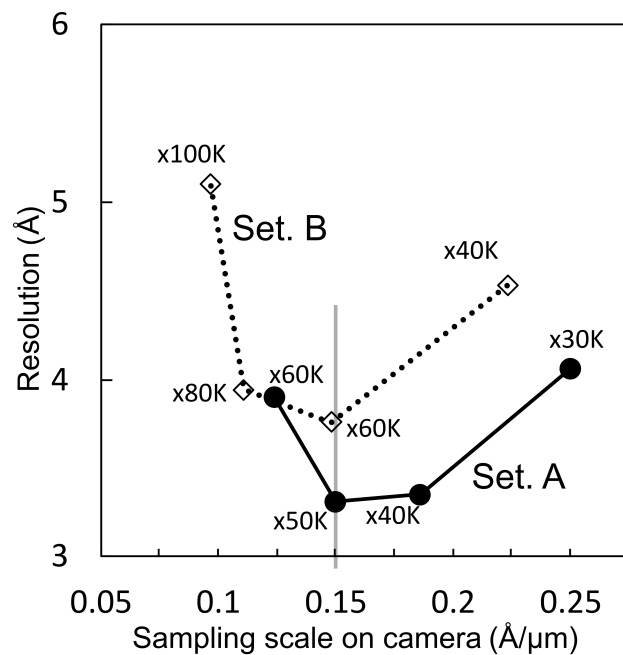
Figure S7. Resolution plots for sampling scales at detector face. Final global estimated resolution of each reconstruction at different magnifications was generated using Settings A and B. Vertical grey line indicates the scaling point at which maximum resolution was achieved for both Settings A and B.

752
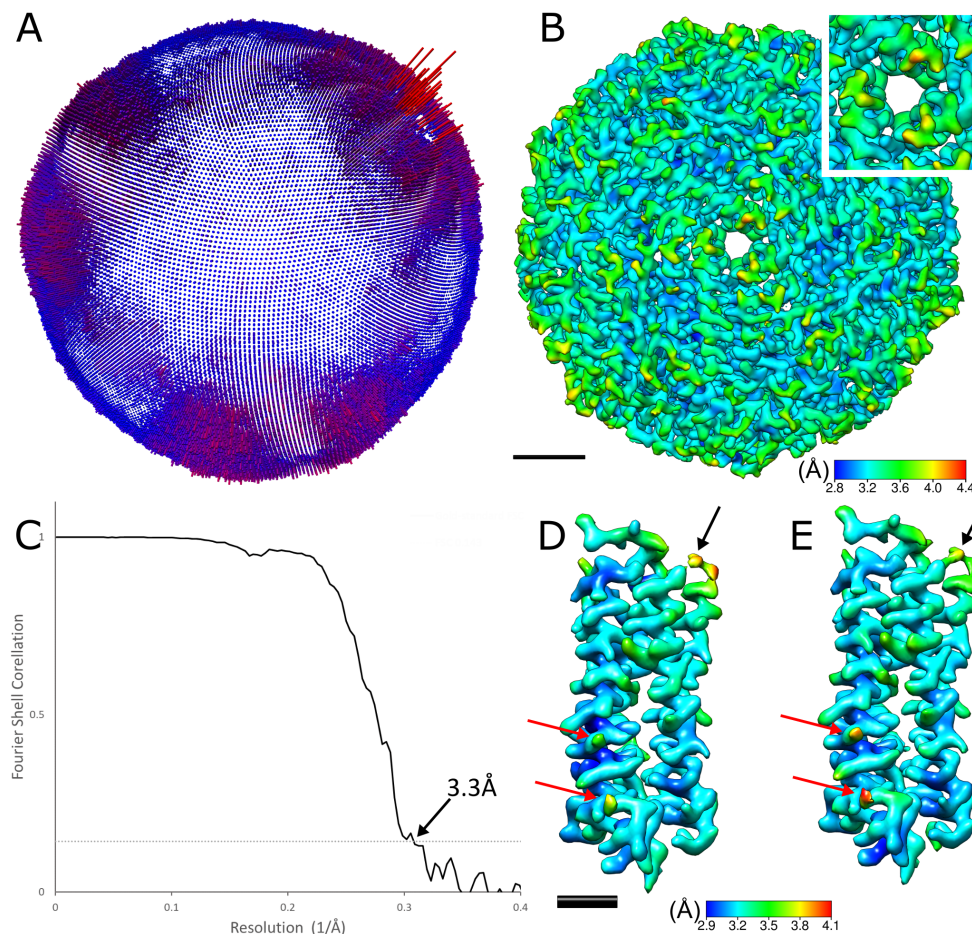
Figure S8. Symmetry expanded reconstruction based upon Setting A 50,000× limited dataset.
The map shows variance in angles assigned, which indicates some asymmetry or flexibility in the protein complex. A) Symmetry expanded angle assignments of apoferritin reconstruction, showing deviation in angular assignment from octahedral symmetry, B) apoferritin reconstruction viewed from same angle as (A) coloured by local resolution observed from the 3-fold symmetry axis, which shows allows example visualisation of resolution variance between three subunits (focussed view in breakout). Scale bars equal 2 nm. C) FSC curve of symmetry expanded apoferritin reconstruction showing 3.3 Å resolution at GS-FSC (0.143). D) extracted subunit from symmetric reconstruction, coloured by local resolution, E) extracted subunit from symmetry expanded (asymmetric) reconstruction, coloured by local resolution. The flexible trans-helix backbone (black arrows in D, E) is contiguous and higher resolution in the asymmetric reconstruction. Some residue sidechains are lower resolution, however (red arrows in D, E). Scale bar equals 1nm.